

# The origin of the LMC stellar bar: clues from the SFH of the bar and inner disk.

L. Monteagudo,<sup>1,2\*</sup> C. Gallart,<sup>1,2</sup> M. Monelli,<sup>1,2</sup> E. J. Bernard,<sup>3</sup> P. B. Stetson<sup>4</sup>

<sup>1</sup>*Instituto de Astrofísica de Canarias (IAC), Calle Vía Láctea s/n, E-38205 La Laguna, Tenerife; Spain*

<sup>2</sup>*Departamento de Astrofísica, Universidad de La Laguna (ULL), E-38206 La Laguna, Tenerife; Spain*

<sup>3</sup>*Université Côte d'Azur, OCA, CNRS, Lagrange, France*

<sup>4</sup>*Herzberg Astronomy and Astrophysics, National Research Council Canada, 5071 West Saanich Road, Victoria, BC V9E 2E7, Canada*

Accepted XXX. Received YYY; in original form ZZZ

## ABSTRACT

We discuss the origin of the LMC stellar bar by comparing the star formation histories (SFH) obtained from deep color-magnitude diagrams (CMDs) in the bar and in a number of fields in different directions within the inner disk. The CMDs, reaching the oldest main sequence turnoffs in these very crowded fields, have been obtained with VIMOS on the VLT in service mode, under very good seeing conditions. We show that the SFHs of all fields share the same patterns, with consistent variations of the star formation rate as a function of time in all of them. We therefore conclude that no specific event of star formation can be identified with the formation of the LMC bar, which instead likely formed from a redistribution of disk material that occurred when the LMC disk became bar unstable, and shared a common SFH with the inner disk thereafter. The strong similarity between the SFH of the center and edge of the bar rules out significant spatial variations of the SFH across the bar, which are predicted by scenarios of classic bar formation through buckling mechanisms.

**Key words:** Hertzsprung–Russel and color–magnitude diagrams – galaxies: evolution – Magellanic Clouds – galaxies: stellar content – galaxies: structure

## 1 INTRODUCTION

The Large Magellanic Cloud is the prototype of a whole class of galaxies, the Barred Magellanic Spirals (SBm), characterized by the presence of an optically visible stellar bar, coincident or not with the dynamical center of the galaxy, a single spiral arm emanating from an end of the bar, and often, a large star forming region at one end of the bar (de Vaucouleurs & Freeman 1972).

The true nature of the bars in these late-type galaxies is the subject of controversy. While in early-type spirals the barred optical morphology is also evident in both the distribution and kinematics of the neutral HI gas, this is not always the case in SBm; in many examples, the bar seems to have a modest effect (if any) on the gas kinematics toward the center of the galaxy (Wilcots 2008).

The existence of the LMC as a very nearby representative of the SBm class offers an excellent opportunity to gain insight on the origin and evolution of these barred structures. In the LMC, a stellar bar is clearly visible in near-IR maps and stellar density

contours (e.g. van der Marel 2001; Cioni et al. 2000) but is not apparent in the HI gas disk (Staveley-Smith et al. 2003; Kim et al. 1998) and is not the site of current star formation as shown by H $\alpha$  images (Kim et al. 1999). There has been a fair amount of discussion regarding its three-dimensional structure (e.g. Zhao & Evans 2000; Zaritsky 2004) and its location with respect to the stellar disk (Subramaniam 2003; Nikolaev et al. 2004; Lah et al. 2005; Koerwer 2009; Subramaniam & Subramaniam 2009).

A few studies have addressed the star-formation history (SFH) of the LMC bar and nearby fields. The high stellar density in the center of the bar, however, has made it difficult to obtain color-magnitude diagrams (CMD) reaching the oldest main sequence turnoffs (oMSTO) with ground-based telescopes, necessary for a reliable determination of the SFH for all ages. The WFPC2 on HST produced the first very deep CMDs of fields in the LMC bar (Elson et al. 1997; Holtzman et al. 1999; Olsen 1999; Smecker-Hane et al. 2002; Weisz et al. 2013), which were populated enough to lead to reliable SFHs; but these were for small portions of the bar and were thus potentially affected by local fluctuations in the stellar populations. Deep and well populated CMDs of the inner LMC disk immediately surrounding the bar region were even more challenging, because a single WFPC2 field typically produced very sparse CMDs. To address this issue, some

\* E-mail: laram@iac.es

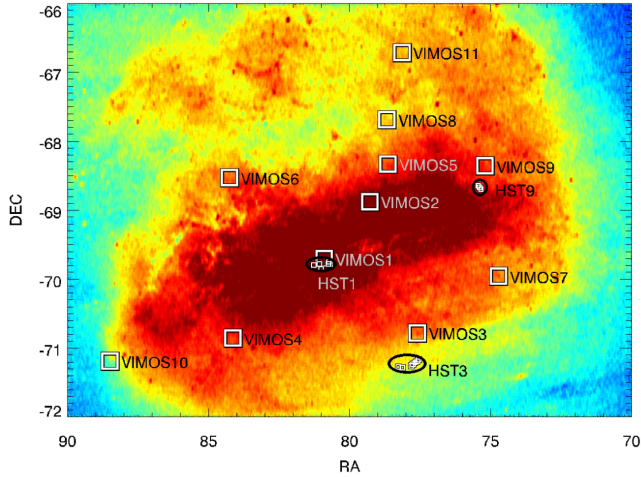


**Figure 1.** Stellar density map of the central region of the LMC, based on the photometry of the Gaia Data Release 1. The location of our VIMOS fields and the archival HST pointings are overlaid.

programs observed mosaics of several WFPC2 fields in the inner LMC disk in different directions from the bar center, and produced CMDs as populated as those in the bar (Smecker-Hane et al. 2002). Comprehensive coverage of the LMC bar and inner disk using the HST, however, remains unfeasible.

For this reason, we have adopted an alternative approach using ground-based observations, taken in excellent seeing conditions with the VLT in service mode. This strategy produces CMDs reaching the oMSTO even in the center of the LMC bar and allows us to study representative portions of the inner LMC for the first time, leading to sound conclusions on their entire SFH. As part of a larger project devoted to an in-depth study of the central LMC SFH and its spatial variations, in this paper we show how the striking similarity of the SFHs of a number of bar and disk fields puts strong constraints on the formation of the LMC bar. This has obvious importance for addressing the long-standing issue regarding the nature of the LMC bar and its possibly differentiated formation and/or evolution.

## 2 OBSERVATIONS AND DATA REDUCTION

We have used the Visible Multi-Object Spectrograph (VIMOS) on the Very Large Telescope (VLT) to obtain deep B and R images in the central part of the LMC. The camera has four CCDs, each with a  $7' \times 8'$  field of view. We observed a total of eleven fields in order to have a significant sampling of the LMC's innermost region. Two fields probe the LMC bar, and the remaining nine fields are distributed in a ring in the inner disk and northern arm within a distance of  $R < 3.2^\circ$  from the bar center. Fig 1 shows the location of these VIMOS fields, superimposed on a stellar density map of the LMC based on data from the Gaia DR1 (Gaia Collaboration et al. 2016).

The observations were designed to reach the oMSTO in the CMD, necessary to obtain a reliable full life-time SFH. They were taken in service mode to ensure the good seeing  $\approx 0.6'' - 0.8''$  necessary to resolve stars down to a faint magnitude limit in these very crowded areas.

We obtained the photometry using DAOPHOT IV and ALL-FRAME (Stetson 1987, 1994). Each chip of each image was reduced independently. Photometric calibration is based on a number of stan-

dard fields observed during a photometric campaign with the CTIO Blanco Telescope, with the MOSAIC camera, on January 15, 2010. In this period we observed the same eleven fields and a number of standard fields, which were selected because of the large number of standard stars available in the database of P.B. Stetson.<sup>1</sup> Finally, a large number of artificial-star tests were performed in each frame following the procedure described in Gallart et al. (1999). These are used both to derive completeness factors and to model photometric errors in the synthetic CMD.

To facilitate the comparison of our SFHs with previous work, we have supplemented our ground-based data with deep archival HST imaging. These HST data are based on WFPC2 images from several programs: GO7382 and GO8576 (P.I. Smecker-Hane), GO7306 (P.I. Cook) and GO6229 (P.I. Trauger). We used photometry and artificial-star tests ( $\sim 1.2 \times 10^5$  per field) taken from the Local Group Stellar Photometry Archive<sup>2</sup> (LGSPA: Holtzman et al. 2006). Fig. 1 shows that the mosaics of disk WFPC2 fields and several WFPC2 fields in the bar are clustered in three small regions of the LMC, which are very close to three of our fields, namely VIMOS1, VIMOS3 and VIMOS9. We have combined the HST observations in three CMDs that we will call HST1, HST3 and HST9 to indicate their closeness to a VIMOS field.

Fig. 2 shows a sample of the VIMOS (left panels) and HST (right) CMDs, for the central bar field (VIMOS1 and HST1 on the top) and one representative disk field (VIMOS3 and HST3). In the case of the bar fields, CMDs from a single WFPC2 pointing contain a number of stars that is sufficient for a robust determination of the SFH (Holtzman et al. 1999; Olsen 1999; Smecker-Hane et al. 2002). For the disk, HST GO programs 7382 and 8576 (see Smecker-Hane et al. 2002) mosaicked 6–10 WFPC2 pointings to obtain CMDs with a number of stars comparable to that of a bar field. These HST CMDs are deeper than the VIMOS ones, but the latter have the advantage of containing a much larger number of stars (see Fig. 2).

An old isochrone has been superimposed on the ground-based CMD of the central bar field (top left panel of Fig. 2) to show that our goal to reach the oMSTO in the CMD was achieved in our most crowded field. To our knowledge, these are the only data taken from the ground with photometry deep enough to reach the oMSTO in the center of the LMC bar. Fig. 2 also shows the *bundles*, or areas of the CMD that have been used to derive the SFH through comparison of the distribution of stars in the observed and synthetic CMDs (see Section 3.1). The number of stars inside the bundles has been labeled in each CMD. Note that, in spite of the fact that several WFPC2 fields have been combined to build the CMDs shown in Fig. 2, the number of stars in the VIMOS CMDs that are relevant for the SFH derivation is many times greater than in the WFPC2 CMDs.

## 3 THE STAR FORMATION HISTORY

### 3.1 SFH Derivation

The SFH calculations for both VIMOS and WFPC2 data were carried out using the CMD-fitting technique, in a way very similar to that described in Aparicio & Hidalgo (2009) and Meschin et al. (2014). We used IAC-star<sup>3</sup> (Aparicio & Gallart 2004) to compute

<sup>1</sup> <http://www3.cadc-ccda.hia-ihp.nrc-cnrc.gc.ca/community/STETSON/standards/>

<sup>2</sup> <http://astronomy.nmsu.edu/holtz/archival/html/lg.html>

<sup>3</sup> <http://iac-star.iac.es>

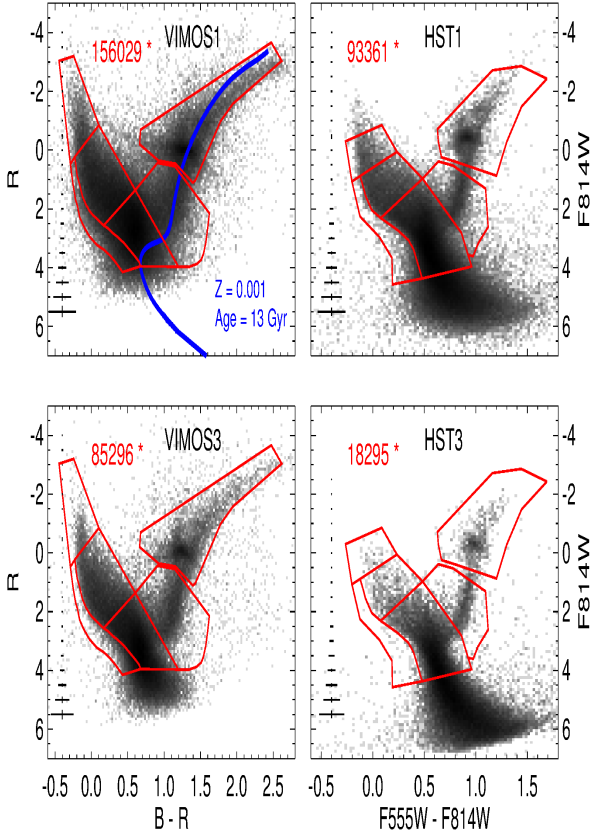


**Figure 2.** **Left panels:** CMDs of two of the VIMOS fields which have a nearby mosaic of WFPC2 data. The blue line in the upper panel is a 13 Gyr old BaSTI isochrone with  $Z=0.001$ ; it highlights that even in the most central, crowded field our photometry is deep enough to reach the  $\alpha$ MSTO. **Right panels:** CMDs of the WFPC2 fields spatially located next to VIMOS fields whose CMDs are displayed in the left panels. Red lines delimit the bundles containing the stars we used for the SFH calculation. The numbers of stars inside the bundles are labeled. Errorbars indicating photometric uncertainties as a function of magnitude are shown in each panel.

a synthetic CMD with a constant star formation rate ( $SFR(t)$ ) between 13.5 and  $\approx 0.03$  Gyr ago;  $5 \times 10^7$  stars in the whole age range are uniformly distributed between  $Z = 0.0001$  and  $0.02$  ( $-2.3 \leq [\text{Fe}/\text{H}] \leq 0.004$ , assuming  $Z_{\odot}=0.0198$ ). The BaSTI stellar evolution library (Pietrinferni et al. 2004, solar scaled, overshooting set) has been adopted. For the initial mass function (IMF) and the binary star distribution function  $\beta(f, q)$  we used the same values as in Meschin et al. (2014): a binary fraction  $f = 0.4$  and a mass ratio distribution  $q > 0.5$ . The IMF was taken from Kroupa (2002) and is given by  $N(m)dm = m^{-\alpha} dm$ , where  $\alpha=1.3$  for stars with mass  $0.1 \leq m/M_{\odot} \leq 0.5$ , and  $\alpha=2.3$  for  $0.5 \leq m/M_{\odot} \leq 100$ .

The incompleteness and photometric uncertainties due to the observational effects have been simulated in the synthetic CMD for each VIMOS and HST pointing based on the results of the corresponding artificial-star tests. In the case of the two bar fields, we identified areas with reddening larger than average and removed the corresponding stars from the CMD used to derive the SFH (approximately one third of the stars were removed for this reason). We verified, however, that the changes in the SFH when including these regions are minimal. No significant effect due to

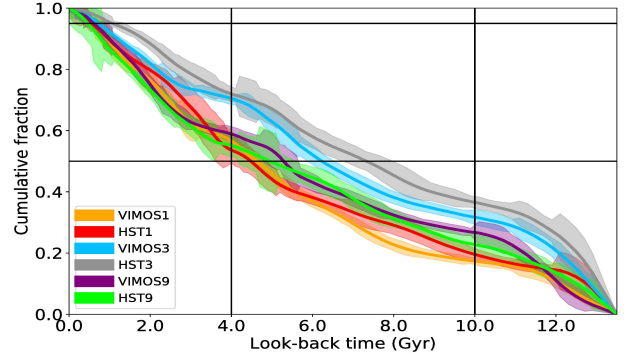


**Figure 3.** Comparison of the cumulative SFHs obtained from the VIMOS and WFPC2 data, for the three LMC regions for which the two data sources are available. The horizontal lines indicate mass fractions corresponding to 50% and 95% of the total accumulated mass. Vertical lines indicate the approximate ages that separate the main star forming episodes mentioned in the text.

differential reddening could be noticed in the CMD of the disk fields. To obtain the SFHs, we used a new algorithm developed in Python by one of us (EJB) (see Bernard et al. 2015, for some details on the algorithm). The same method was applied to all the VIMOS fields and three HST groups.

### 3.2 Comparison of VIMOS and HST SFHs

In this section we compare the SFH of the two VIMOS fields located next to HST ones to show that the SFHs derived from the VIMOS data are compatible with those obtained from the deeper HST data. The results, in the form of cumulative SFHs, are displayed in Fig. 3. It can be seen that the SFHs for each VIMOS and corresponding WFPC2 field are basically identical within the errors, while there are noticeable differences between fields. The largest difference in photometric depth between the VIMOS and corresponding WFPC2 field occurs for the bar field (#1), for which the VIMOS CMD reaches just about half a magnitude below the  $\alpha$ MSTO. The results in Fig. 3, however, show that the features in the SFH are equally recovered from both CMDs. The much larger number of stars in the less deep VIMOS CMD and, particularly, the fact that it does reach the  $\alpha$ MSTO, are likely the key reasons for this.

### 3.3 The SFH of the LMC bar and inner disk from VIMOS data

We obtained SFHs for each individual VIMOS field and compared them. The detailed results on individual fields, including both  $SFR(t)$  and age-metallicity relations, will be presented in a future paper (Monteagudo et al. 2018, in preparation). Disk fields #3, 4, 5, 6, 7, 8 and 10 have very similar SFHs, characterized by relatively smooth variations of the  $SFR(t)$  with respect to a mean value, over the whole lifetime of the galaxy, resulting in a cumulative  $SFR(t)$  close to a constant value. Therefore, for clarity in Fig. 3 we only show the SFH of field #3. The SFH of the two bar fields indicates a stellar population younger overall, while that of disk fields #9 and 11 (see SFH for field #9 in Fig. 3) is somewhat intermediate between the remaining disk fields and the bar fields. Since these two fields are located in the North LMC arm, we will exclude them from the upcoming analysis, focused on the comparison of the SFHs of the

bar and inner disk. However, including them in the analysis would not change the conclusions of the paper.

In this paper, we are interested in exploring possible variations of the SFH within the bar, and between the bar and the surrounding inner disk fields. Therefore, for the purposes of the current paper, we have combined the CMDs of disk fields with similar SFHs into three CMDs that we will consider representative of the stellar populations of the inner disk in the N, E, and SW directions. DiskE will correspond to fields with  $\alpha_{2000} \geq 05:30:00$  (VIMOS4+6+10), DiskSSW to fields with  $\alpha_{2000} \leq 05:10:00$  and  $\delta_{2000} \geq -68:00:00$  (VIMOS3+7) and DiskN to those with  $\alpha_{2000} \simeq 05:14:00$  (VIMOS5+8). For the bar fields (#1 and #2) we have computed individual SFHs, which are represented in the upper panel of Fig. 4 in cumulative form. Note that both are almost identical within the errors (with the SFH for the central bar field marginally younger than that of the field in the NW extreme of the bar) indicating a basically common SFH for the whole bar. We have thus combined both bar fields for further comparison with the disk. These comparisons are shown in the middle and lower panel of Fig. 4 in cumulative and time resolved form respectively. In all figures, the SFHs are represented with their corresponding uncertainties, estimated following the prescriptions of Hidalgo et al. (2011).

The lower panel of Fig. 4 shows that the SFR(t) of the bar and combined disk fields presents common features and consistent trends. All are characterized by three main periods of star formation separated by short gaps of almost negligible star formation activity. We find an early star formation episode (*old star-forming epoch*,  $O_{SFE}$ ) common to all fields and lasting  $\simeq 3.5$  Gyr. A second period of enhanced SFR(t) (*intermediate star-forming epoch*,  $I_{SFE}$ ) is found between 10 and 4 Gyr ago. Finally, the most recent period (*young star-forming epoch*,  $Y_{SFE}$ ) began  $\sim 4$  Gyr ago. Within each period, there are variations in the intensity of the SFR(t) which are only slightly different in detail from field to field. In particular, it is interesting to note that, within the young star-forming epoch, which is the one for which we can be most confident on the details of SFR(t), there are variations that are totally consistent among all fields. Three peaks of star formation activity are observed at  $\simeq 2.5$ , 1.0 and 0.5 Gyr ago, while star formation appears very much reduced at the present time.

What is different between bar and disk fields is the relative number of stars formed in the three main epochs of star formation. In the first three lines of Tab. 1 we indicate the fraction of stars formed in each of them, for the combined bar fields and disk fields. The fraction of stars formed in the  $O_{SFE}$  is lower in the bar field than in the disk fields, and the contrary is true for the  $Y_{SFE}$ , while the fraction formed at intermediate ages is similar in all fields. This leads to a ratio Y/O and Y/(I+O) about a factor of two larger in the bar compared to the disk. These differences are reflected in the respective cumulative mass fractions, displayed in the middle panel of Fig. 4. In this figure, the two horizontal lines indicate the 50 and 95 mass percentiles. The ages at which these percentiles are reached in each field are listed in Tab. 1. They indicate that the disk formed half of its mass between 1.25 and 2 Gyr earlier than the bar.

### 3.4 Discussion: the origin of the LMC bar

The highly detailed SFHs that we have derived for a number of regions covering representative portions of the LMC bar and inner disk allow us to provide important constraints on the nature of the LMC bar. In the previous section we have shown that the SFHs of the bar and disk fields closely share the same features, and thus, *no event of star formation can be identified with the formation of the*

**Table 1.** Derived values from the SFH

	Bar	Disk E	Disk SW	Disk N
$Y_{SFE}$	0.50±0.03	0.40±0.02	0.33±0.02	0.35±0.02
$I_{SFE}$	0.31±0.03	0.31±0.02	0.37±0.03	0.34±0.03
$O_{SFE}$	0.19±0.02	0.28±0.03	0.30±0.03	0.30±0.05
$(Y/O)_{SFE}$	2.6±0.3	1.45±0.18	1.12±0.13	1.16±0.21
$(Y/(I+O))_{SFE}$	1.00±0.09	0.68±0.05	0.49±0.04	0.55±0.07
$T_{50\%}$ (Gyrs)	4.25	5.5	6.25	6.25
$T_{95\%}$ (Gyrs)	0.5	0.75	0.75	1.00

*LMC bar*. This conclusion is different from that reached in previous studies (Elson et al. 1997; Smecker-Hane et al. 2002). In particular, Smecker-Hane et al. (2002) identified a 4–6 Gyr star formation episode with the formation of the LMC bar. The significantly larger fields, covering different positions in the LMC inner regions, and the more sophisticated analysis technique (Smecker-Hane et al. 2002, simply modeled the main sequence luminosity function to derive the SFH), makes us confident that our conclusion is robust. It implies that the bar likely formed from a redistribution of disk material that occurred when the disk became bar unstable, and shared a common SFH with the inner disk thereafter.

The fact that the  $Y_{SFE}$  has been somewhat more intense in the bar (and in its innermost region) than in the inner disk might be a consequence of younger, colder material and gas being preferentially funneled to the center of the galaxy by the non-axisymmetric potential. However, it may also simply be a continuation of the gradient seen in the outer disk (Gallart et al. 2008; Meschin et al. 2014), and common in dwarf irregular galaxies (e.g. Bernard et al. 2007; Stinson et al. 2009; Hidalgo et al. 2013) in the sense that younger populations are concentrated toward the central parts of the galaxies.

The fact that the two bar fields, one located in its very center and the other on its northern rim, also share a closely similar SFH allows us to put further constraints on the characteristics of the LMC bar. Friedli & Benz (1995) showed that the formation of a strong bar in a typical Sc disk induces a significant starburst in the bar and in the galactic center. The lack of an excess of  $H\alpha$  emission in the bar region (Kim et al. 1999) indicates that such a starburst is not currently ongoing and our SFH results allow us to reach the same conclusion for the rest of the galaxy’s lifetime. This kind of predicted variations of the SFH within the bar caused by bar formation and buckling have been recently observed in the SBb galaxy NGC 6032, where it was also observed that the SFH of the outer bar was similar to that of the disk (Pérez et al. 2017). The basically identical SFH across the LMC bar points to the absence of these buckling mechanisms characteristic of classical bars in more massive galaxies. A more comprehensive mapping of the SFH across the whole LMC bar is necessary to confirm this point, which places important constraints on the formation of bars in low mass galaxies, particularly of the Magellanic type.

### ACKNOWLEDGEMENTS

We thank I. Pérez, I. Martínez-Valpuesta and T. Ruíz-Lara for useful discussions. This research is based on observations made with the ESO VLT at the La Silla Paranal Observatory under programme ID 084.B-1124, and in observations made with the NASA/ESA Hubble Space Telescope, obtained from the data archive at the Space Telescope Science Institute. STScI is operated by AURA under NASA contract NAS 5-26555. This work has been supported by

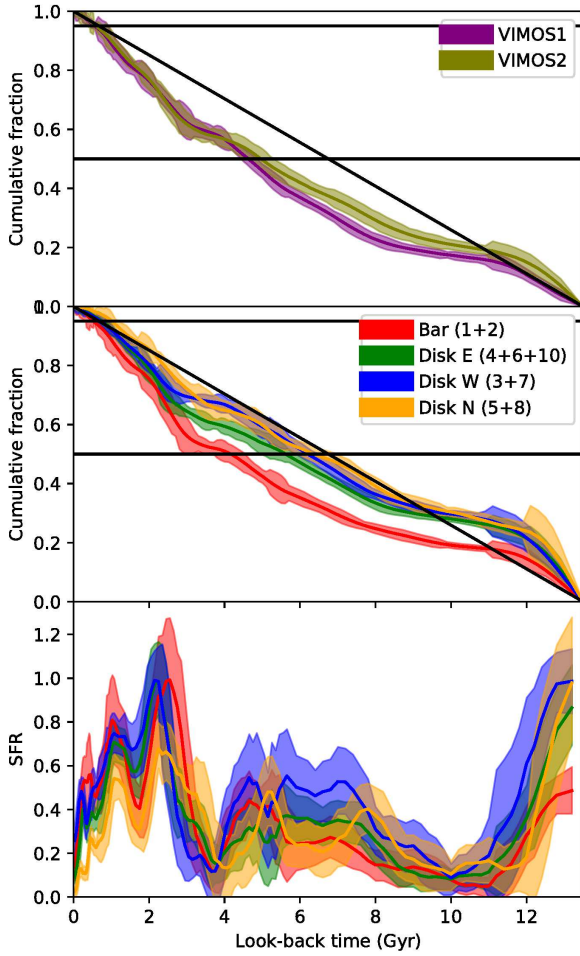


**Figure 4. Top panel:** Cumulative SFH for the LMC bar fields, #1 and #2. The horizontal lines indicate mass fractions corresponding to 50% and 95% of the total accumulated mass. **Middle and lower panels:** SFHs (in cumulative and time resolved form, respectively) for the bar and disk fields, grouped as indicated in the text.

the Spanish Ministry of Economy and Competitiveness (MINECO) under grant AYA2014-56795-P. EJB acknowledge support from the CNES postdoctoral fellowship program.

## REFERENCES

Aparicio A., Gallart C., 2004, *AJ*, **128**, 1465  
 Aparicio A., Hidalgo S. L., 2009, *AJ*, **138**, 558  
 Bernard E. J., Aparicio A., Gallart C., Padilla-Torres C. P., Panniello M., 2007, *AJ*, **134**, 1124  
 Bernard E. J., Ferguson A. M. N., Chapman S. C., Ibañez R. A., Irwin M. J., Lewis G. F., McConnachie A. W., 2015, *MNRAS*, **453**, L113  
 Cioni M.-R. L., Habing H. J., Israel F. P., 2000, *A&A*, **358**, L9  
 Elson R. A. W., Gilmore G. F., Santiago B. X., 1997, *MNRAS*, **289**, 157  
 Friedli D., Benz W., 1995, *A&A*, **301**, 649  
 Gaia Collaboration et al., 2016, *A&A*, **595**, A2  
 Gallart C., Freedman W. L., Aparicio A., Bertelli G., Chiosi C., 1999, *AJ*, **118**, 2245  
 Gallart C., Stetson P. B., Meschin I. P., Pont F., Hardy E., 2008, *ApJ*, **682**, L89  
 Hidalgo S. L., et al., 2011, *ApJ*, **730**, 14

Hidalgo S. L., et al., 2013, *ApJ*, **778**, 103  
 Holtzman J. A., et al., 1999, *AJ*, **118**, 2262  
 Holtzman J. A., Afonso C., Dolphin A., 2006, *ApJS*, **166**, 534  
 Kim S., Staveley-Smith L., Dopita M. A., Freeman K. C., Sault R. J., Kesteven M. J., McConnell D., 1998, *ApJ*, **503**, 674  
 Kim S., Dopita M. A., Staveley-Smith L., Bessell M. S., 1999, *AJ*, **118**, 2797  
 Koerwer J. F., 2009, *AJ*, **138**, 1  
 Kroupa P., 2002, *Science*, **295**, 82  
 Lah P., Kiss L. L., Bedding T. R., 2005, *MNRAS*, **359**, L42  
 Meschin I., Gallart C., Aparicio A., Hidalgo S. L., Monelli M., Stetson P. B., Carrera R., 2014, *MNRAS*, **438**, 1067  
 Nikolaev S., Drake A. J., Keller S. C., Cook K. H., Dalal N., Griest K., Welch D. L., Kanbur S. M., 2004, *ApJ*, **601**, 260  
 Olsen K. A. G., 1999, *AJ*, **117**, 2244  
 Pérez I., et al., 2017, *MNRAS*, **470**, L122  
 Pietrinferni A., Cassisi S., Salaris M., Castelli F., 2004, *ApJ*, **612**, 168  
 Smecker-Hane T. A., Cole A. A., Gallagher III J. S., Stetson P. B., 2002, *ApJ*, **566**, 239  
 Staveley-Smith L., Kim S., Calabretta M. R., Haynes R. F., Kesteven M. J., 2003, *MNRAS*, **339**, 87  
 Stetson P. B., 1987, *PASP*, **99**, 191  
 Stetson P. B., 1994, *PASP*, **106**, 250  
 Stinson G. S., Dalcanton J. J., Quinn T., Gogarten S. M., Kaufmann T., Wadsley J., 2009, *MNRAS*, **395**, 1455  
 Subramaniam A., 2003, *Bulletin of the Astronomical Society of India*, **31**, 413  
 Subramaniam A., Subramanian S., 2009, *ApJ*, **703**, L37  
 Weisz D. R., Dolphin A. E., Skillman E. D., Holtzman J., Dalcanton J. J., Cole A. A., Neary K., 2013, *MNRAS*, **431**, 364  
 Wilcots E. M., 2008, *Astrophysics and Space Science Proceedings*, **5**, 69  
 Zaritsky D., 2004, *ApJ*, **614**, L37  
 Zhao H., Evans N. W., 2000, *ApJ*, **545**, L35  
 de Vaucouleurs G., Freeman K. C., 1972, *Vistas in Astronomy*, **14**, 163  
 van der Marel R. P., 2001, *AJ*, **122**, 1827

This paper has been typeset from a  $\text{\LaTeX}$  file prepared by the author.